Gondwana Research 46 (2017) 114–123

Contents lists available at ScienceDirect

Gondwana Research

journal homepage: www.elsevier.com/locate/gr

Structure and magnitude of the carbon isotope excursion during the Paleocene-Eocene thermal maximum

Qinghai Zhang [a,b,*], Ines Wendler [a], Xiaoxia Xu [a], Helmut Willems [a,c], Lin Ding [b]

[a] Department of Geosciences, University of Bremen, 28359 Bremen, Germany
[b] Key Laboratory of Continental Collision and Plateau Uplift, Institute of Tibetan Plateau Research, Centre for Excellence in Tibetan Plateau Earth Sciences, Chinese Academy of Sciences, 100101 Beijing, China
[c] Nanjing Institute of Geology and Palaeontology, Chinese Academy of Sciences, 210008 Nanjing, China

ARTICLE INFO

Article history:
Received 20 August 2016
Received in revised form 12 December 2016
Accepted 25 February 2017
Available online 22 March 2017

Handling Editor: J.G. Meert

Keywords:
PETM
Tibet
Bulk carbonate
CIE profile
CIE magnitude

ABSTRACT

The Paleocene-Eocene Thermal Maximum (PETM) was a geologically rapid and transient warming event that occurred ca. 56 million years ago (Ma). It was associated with a pronounced negative carbon isotope excursion (CIE) and with profound changes in the atmosphere, hydrosphere and biosphere. This event reflects injections of large amounts of carbon into the atmosphere-ocean system, but, whether single or multiple episodes of carbon release caused this event is uncertain. Here, we present carbon isotope data of bulk carbonate from two parallel limestone sections at Tingri (south Tibet), where the limestone was deposited on a tropical carbonate ramp during the PETM. Carbon isotope data of bulk carbonate from both sections are almost identical, displaying an expanded stepped CIE profile with large magnitude. The stepped CIE profile consists of three discrete intervals of decreasing carbon isotope values, which can be correlated on an inter-regional scale between sections from different depositional environments (lake, carbonate ramp, continental slope, and open ocean). The consistency of these correlations implies occurrence of at least three carbon releases within the CIE and indicates complex processes of carbon injection during the PETM. Moreover, the CIE magnitude of ~7‰ recorded at Tingri is tentatively interpreted to reflect carbon isotope changes in the atmosphere and the surface ocean, which is larger than the generally accepted value of ~4‰ but is still within the range of some previous records.

1. Introduction

A geologically rapid event characterized by profound changes in biotic evolution, climate and geochemical cycling occurred at the Paleocene-Eocene transition. During this event, now called the Paleocene-Eocene Thermal Maximum (PETM), global temperature increased by >4 °C (Dunkley Jones et al., 2013; Zachos et al., 2003) within several thousand years (Farley and Eltgroth, 2003; Röhl et al., 2007). This warming event was accompanied by a global negative CIE of ~2–8‰ (McInerney and Wing, 2011) and severe carbonate dissolution on the ocean floor (Zachos et al., 2005; Zeebe et al., 2009). The combination of the CIE and carbonate dissolution indicates that a large amount of ^{13}C–depleted carbon was injected into the atmosphere-ocean system, resulting in strong perturbations of the global carbon cycle (Dickens et al., 1995). Moreover, concurrence of the global warming and carbon perturbations suggests a causal relationship between carbon injections and the PETM. In order to better understand the causes of the PETM, it is important to constrain the timing, magnitude and nature of the carbon injection(s) (Cui et al., 2011; DeConto et al., 2012; Dickens et al., 1995; Higgins and Schrag, 2006; Svensen et al., 2004; Wright and Schaller, 2013).

While the duration of the CIE is relatively well constrained (Farley and Eltgroth, 2003; Röhl et al., 2007), its magnitude suggested from different substrates varies considerably (McInerney and Wing, 2011; Sluijs and Dickens, 2012), and structure of the complete CIE profile remains the subject of much debate (Bains et al., 1999; Chen et al., 2014; Manners et al., 2013; Zhu et al., 2010). Comparatively, recognition of the complete CIE profile is crucial, because: (1) the full duration and magnitude of the CIE can only be acquired from sections that preserve the complete CIE profile, and (2) the complete CIE profile can reveal details on phases of carbon release during the PETM.

Generally, two different types of the CIE profile have been discussed in the literature: a simple triangular CIE profile and a more complex stepped CIE profile (Fig. 1). The triangular CIE profile is characterized by a single large decrease in $\delta^{13}C$ values, followed by an exponential recovery. This type is recorded in a variety of substrates from marine and terrestrial sections, including foraminifera, bulk carbonate, organic matter and algal lipids (McInerney and Wing, 2011). In contrast, the stepped CIE profile typically consists of three phases of decreasing $\delta^{13}C$ values separated by intervals of relatively stable $\delta^{13}C$, followed by

* Corresponding author at: Department of Geosciences, University of Bremen, 28359 Bremen, Germany.
E-mail address: zhang@uni-bremen.de (Q. Zhang).

http://dx.doi.org/10.1016/j.gr.2017.02.016
1342-937X/

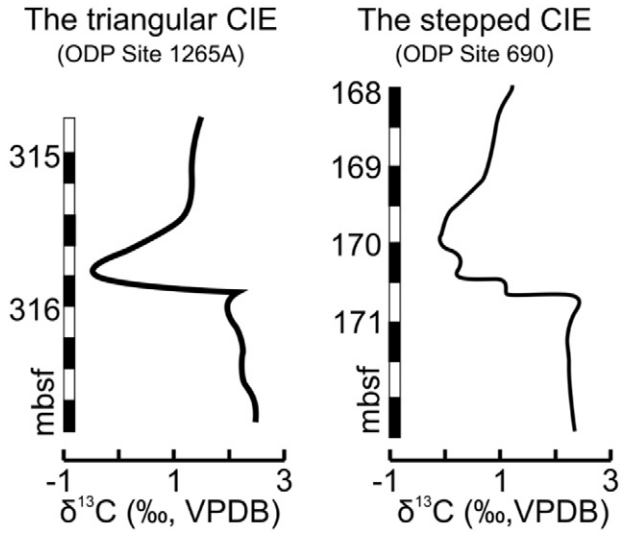

Fig. 1. Two different types of the CIE profile during the PETM as exemplified by $\delta^{13}C$ variations of bulk carbonate at ODP Sites 1265A and 690. mbsf = meter below sea floor; VPDB = Vienna Peedee Belemnite.

an exponential recovery. This CIE profile is well exemplified in the bulk carbonate $\delta^{13}C$ record at Ocean Drilling Program (ODP) Site 690 (Bains et al., 1999).

If the stepped CIE profile represents a complete record of carbon perturbations during the PETM, the triangular CIE profile must represent an incomplete or disturbed CIE record, which could result from: (1) truncation owing to carbonate dissolution, (2) condensation caused by slow sedimentation rates, (3) smoothing of species-specific data due to bioturbation (Zachos et al., 2007), (4) low-resolution sampling, (5) diagenetic overprint or other processes. Alternatively, the stepped CIE profile at ODP Site 690 could be an artifact of sediment reworking and/or mixing of different components of nannoplankton species (Bralower, 2002). In such a case, reproduction of the stepped CIE profile from other sections will be nearly impossible, due to the complexness of the stepped CIE profile and stochastic processes of reworking and mixing. Classically, the stepped CIE profile was thought to result from multiple phases of carbon release (Bains et al., 1999), whereas the triangular CIE profile reflects a single carbon release event. So, whether or not the stepped CIE profile is an artifact has great significance for understanding carbon perturbations during the PETM.

Although ODP Site 690 was regarded as the reference section for the PETM (Kennett and Stott, 1991), the validity of the stepped CIE profile recorded in its bulk carbonate has been called into question, on the basis of two lines of evidence: (1) the $\delta^{13}C$ measurements of both planktonic and benthic foraminifera from the same section cannot reproduce the stepped CIE profile (Thomas et al., 2002), and (2) the stepped CIE profile was thought to be caused by vital effects of nannoplankton (Bralower, 2002). Although some low-resolution $\delta^{13}C$ records with the CIE structures similar to that from ODP Site 690 were reported from other hemipelagic/pelagic sections (ODP Sites 1051 and 1263, DSDP Site 277 and Mead Stream) (Bains et al., 1999; Hollis et al., 2015; Nicolo et al., 2010; Zachos et al., 2005) and interspecific vital effects of the Paleocene coccolith were demonstrated to be very small (Stoll, 2005), the issue about the primary nature of the stepped CIE remains unresolved, because an expanded, high-resolution stepped CIE profile has not been observed so far.

To date, the PETM has been studied from numerous shallow-marine siliciclastic and hemipelagic/pelagic sections (McInerney and Wing, 2011). However, some shallow-marine carbonate sections are probably ideal for studying the CIE profile. Compared to pelagic sediments, shallow-marine carbonates deposited on carbonate platforms/ramps were formed at higher sedimentation rates and can avoid the effect of carbonate dissolution. Thus, they have the potential to preserve expanded CIE records, if accommodation space was large enough for continuous sedimentation. Compared to shallow-marine siliciclastic sediments, carbonates are formed in the depositional environment that is less affected by terrestrial input (e.g., river runoff), which can facilitate the preservation of primary signals of carbon isotope variations in the ocean.

In this study, we present the first records of carbon isotope composition of bulk carbonate ($\delta^{13}C_{carb}$) and wt% $CaCO_3$ (weight percentage) from two parallel limestone sections (13ZS and 10/11TM) at Tingri (south Tibet), and the $\delta^{13}C_{carb}$ data show that an expanded CIE profile is preserved in this area. Then, we use data of Sr and Mn concentrations and $^{87}Sr/^{86}Sr$ ratios to exclude the possibility of diagenetic alteration. After that, the effect of mixed components on the $\delta^{13}C_{carb}$ records is qualitatively evaluated. By comparing the background $\delta^{13}C_{carb}$ values at Tingri with the background $\delta^{13}C$ values of mixed-layer foraminifer *Acarinina* from different ODP Sites, we confirm that the $\delta^{13}C_{carb}$ records from the shallow epicontinental sea of the Tingri area can reflect the carbon cycling in the open surface ocean. In the end, we discuss the stepped CIE profile and the CIE magnitude during the PETM.

2. Geological background

During the Paleocene and early Eocene, Tingri (south Tibet) was located in the Tethyan Himalaya of the northern Greater Indian continental margin (Fig. 2), where thick carbonate sequences of the Zhepure Shan Formation were deposited on a tropical carbonate ramp (Willems et al., 1996; Zhang et al., 2013). To the south of the Tethyan Himalaya, contemporary shallow marine strata of the Subathu Formation crops out in the Lesser Himalaya (Najman, 2006), indicating that the southern shoreline of the Neo-Tethyan Ocean was located either within the Lesser Himalaya or even to the south. By taking into account the post-55 Ma shortening of the upper crust in the Himalaya (DeCelles et al., 2002), Tingri was at least ~300 km away from the shoreline during the PETM.

The carbonate rocks of the Zhepure Shan Formation comprise four lithological members (Members A to D; Fig. 3a), the upper three of which are rich in larger benthic foraminifera. Based on the larger foraminifera, ten Shallow Benthic Zones (SBZ) were distinguished in the Zhepure Shan Formation (Zhang et al., 2013). Integration of bio- and chemostratigraphy enabled identification of the Paleocene-Eocene (P/E) boundary within a nodular limestone in the upper part of the Member C (Zhang et al., 2013) (Fig. 3b).

We studied two parallel sections (10/11TM and 13ZS), at a distance of ~50 m, in order to test for lateral consistency of the $\delta^{13}C_{carb}$ variations and evaluate the effect of mixed different components on the $\delta^{13}C_{carb}$ records. Two sections cover a stratigraphic interval from the latest Paleocene to the earliest Eocene. The lower part of the sections is rich in lamellar-perforate larger foraminifera of the genera *Lockhartia*, *Miscellanea*, *Kathina*, *Operculina* and *Ranikothalia*, which typically appeared in the late Paleocene to the earliest Eocene (Serra-Kiel et al., 1998; Zhang et al., 2013) and indicated a paleo-bathymetry of ~40–80 m (Hottinger, 1997). At ~18.6 m of the sections, a sudden biotic change from lamellar-perforate foraminifera to porcellaneous-walled *Alveolina* occurs, suggesting a shoaling of the depositional environment to <40 m (Hottinger, 1997) (Fig. 4).

Rocks in this PETM-CIE interval are composed of calcareous marl, marly nodular limestone and nodular limestone. The main interval of the CIE is recorded in the nodular limestone, which is non-stratified and mainly consists of decimeter-sized, sub-rounded nodules. The nodules are similar in size and are separated by very thin marly matrix. They are densely packed and show a fitted-fabric texture. Overall, its appearance displays a high extent of homogeneity (Fig. 3b).

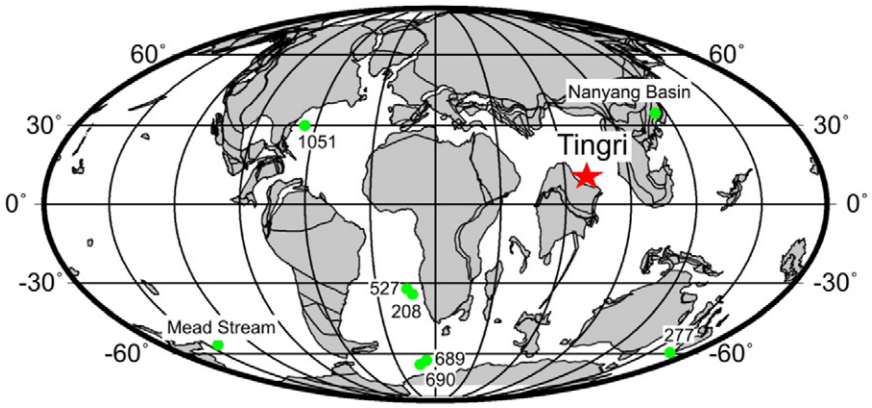

Fig. 2. Paleogeographic reconstruction (56 Ma; from ODSN Plate Tectonic Reconstruction Service) showing locations of the studied sections (red star) and other PETM sections (green dots). The latter includes ODP Sites 690, 689, 527 and 1051, ODP Leg 208 with Sites 1262 to 1267, Deep Sea Drilling Project (DSDP) Site 277, Mead Stream in New Zealand and Nanyang Basin in China.

3. Materials and methods

Both sections were sampled at a spacing of ~20 cm in the field. In the laboratory, thin-sections were prepared for all samples in order to observe changes of the larger benthic foraminiferal assemblage and qualitatively evaluate the degree of diagenesis through cathodoluminescence examination. For geochemical analysis, samples were cut to expose fresh surfaces, where diagenetically less-altered micrites and fragments of the larger foraminifera were carefully micro-drilled under a light microscope (Fig. 5). Veins, vugs and petrographically visible diagenetic parts were strictly avoided. About 20 g of material was obtained from each sample and then was ground to powder in an agate mortar for geochemical analysis. The $\delta^{13}C_{carb}$ and wt% $CaCO_3$ have been analyzed in section 13ZS while in section 10/11TM only the $\delta^{13}C_{carb}$ was measured. Besides, 16 samples from section 10/11TM were randomly selected to analyze the $^{87}Sr/^{86}Sr$ ratios, Sr and Mn concentrations. All measurements were carried out in the Department of Geosciences and MARUM Center for Marine Environmental Sciences, University of Bremen.

3.1. Analysis of $\delta^{13}C_{carb}$ and $\delta^{18}O_{carb}$

About 50–150 μg of rock powder were reacted with phosphoric acid at 75 °C in an automated carbonate unit. The CO_2 was measured with a Finnigan MAT 251 gas isotope ratio mass spectrometer. The data were calibrated against a laboratory standard (Solnhofen limestone), and the latter was calibrated against the NBS 19 carbonate international standard. All isotope-ratio data are reported in ‰ versus VPDB (Vienna Peedee Belemnite). Based on replicate measurements of the laboratory standard, reproducibility (±1 SD) for $\delta^{13}C$ values and for $\delta^{18}O$ values is ±0.05‰ and ±0.07‰, respectively.

3.2. Analysis of wt% $CaCO_3$

An empty 40 ml vial was weighed by using an analytical balance (W_{vial}). Then, about 3 g of rock powder was added in the vial, and the vial was weighed again ($W_{vial\ +\ rock}$). After that, 10% HCl (*w*/*v*) was added in the vial and reacted with rock powder for 24 h to dissolve carbonate completely. The residue was centrifuged repeatedly and rinsed with deionized distilled water to a pH value of ~5–6, and freeze-dried. The vial was weighed once again ($W_{vial\ +\ residue}$). The $CaCO_3$ wt% was calculated with the following equation: wt% $CaCO_3 = (W_{vial\ +\ rock} - W_{vial\ +\ residue})/(W_{vial\ +\ rock} - W_{vial}) \times 100\%$.

3.3. Analysis of Sr and Mn concentrations

Analyses of Sr and Mn concentrations were carried out on thin sections by laser ablation inductively coupled plasma mass spectrometry (LA-ICP-MS), using a Thermo Element 2 coupled to a New Wave UP193ss (wavelength 193 nm). Helium (0.8 l/min) was used as carrier gas and argon (0.8–0.9 l/min) was added as make-up gas; plasma power was 1200 W. Formation of oxides in the plasma was low (ThO/Th ca. 0.15%) so that no interference correction for the elements was applied. Samples and standards were ablated with an irradiance of ~1 GW/cm^2, a spot diameter of 75 μm and a pulse rate of 5 Hz. Prior to ablation the blank intensities were acquired during 25 s. All isotopes were analyzed at low resolution with five samples in a 20% mass window and a total dwell time of 25 ms per isotope. NIST610 glass was analyzed as external calibration standard for every 10 samples. For data

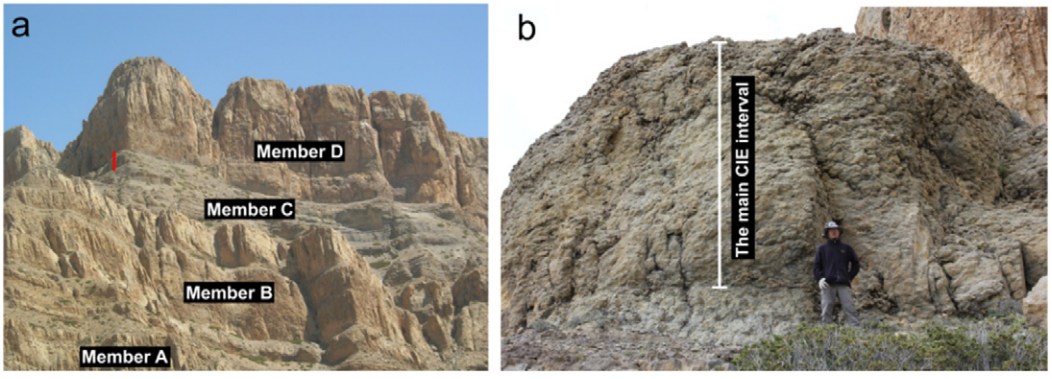

Fig. 3. Photographs of the studied sections at Tingri. (a) The Paleocene-lower Eocene Zhepure Shan Formation with four lithological members and the location of section 13ZS (red bar). (b) Close-up of the interval recording the main CIE of the PETM.

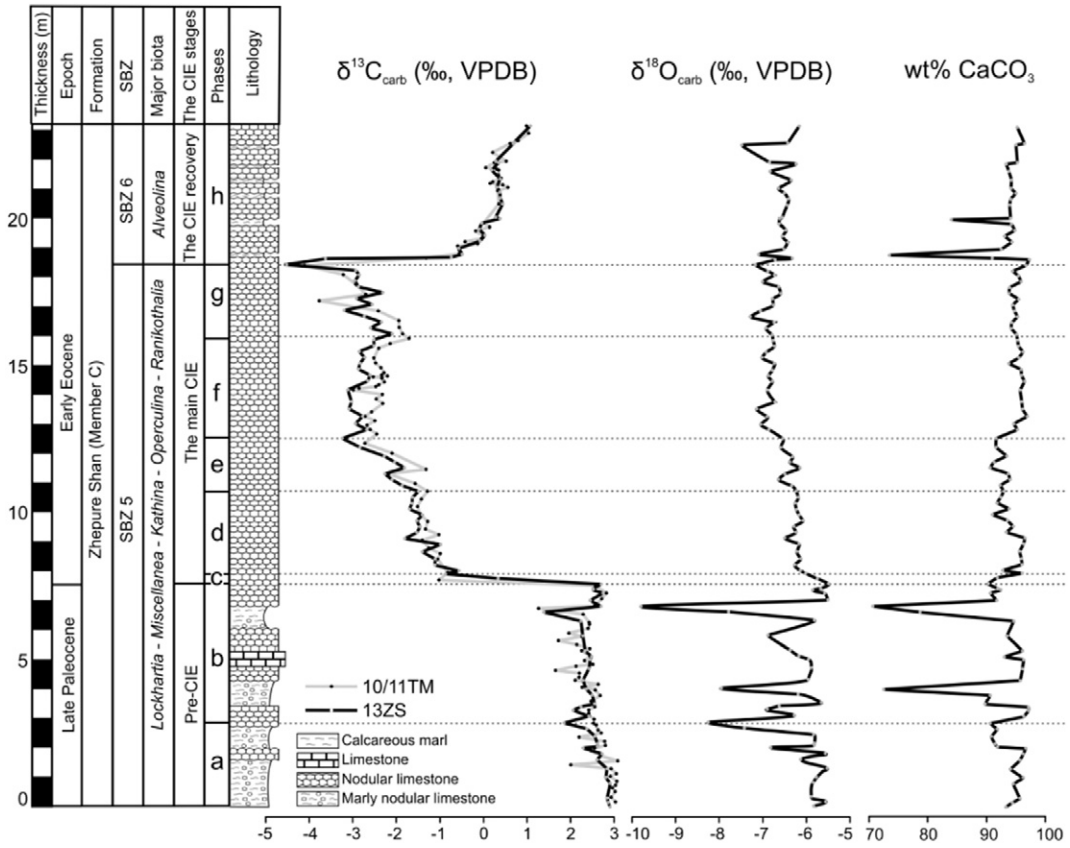

Fig. 4. Lithology, biostratigraphy, and variations in $\delta^{13}C_{carb}$, $\delta^{18}O_{carb}$, and wt% $CaCO_3$ from section 13ZS at Tingri with additional $\delta^{13}C_{carb}$ data from a parallel section (section 10/11TM; grey curve). The SBZ and major biota are from Zhang et al. (2013), and different phases of $\delta^{13}C_{carb}$ variations are denoted by lower-case letters and are delimited by dashed lines.

quantification, the Cetac GeoPro™ software was used with ^{43}Ca as internal standard. Ca concentrations in carbonates were determined by normalizing the analyzed Ca, Mg, Fe, Si and Al contents to $(Ca + Mg + Fe)CO_3 + SiO_2 + Al_2O_3 = 100$ wt%, i.e., assuming that Ca, Mg and Fe are fixed as carbonate and Si and Al as oxide or silicate. Data quality was assessed by repeated analyses of USGS reference materials BHVO2G, BCR2G (basalt glasses), and MACS3 (carbonate) along with the samples. The mean deviation from the reference values (GeoReM data base, MPI Mainz) is <10% for most elements. External precision is better than 5% for the elements, as determined by consecutive analyses of NIST614 glass.

3.4. Analysis of $^{87}Sr/^{86}Sr$ ratios

The $^{87}Sr/^{86}Sr$ ratios of bulk carbonate were analyzed by thermal ionization mass spectrometry (TIMS) on a Triton plus instrument (Thermo Scientific). About 20 mg of rock powder was dissolved in double distilled 3 mol HNO_3, dried, and re-dissolved in 600 μl of 2 mol HNO_3 for chemical separation. Strontium was isolated from the matrix elements by using miniaturized columns with 70 μl of Sr specific resin (Sr.spec 50–100 μm particle size by TrisKem® International/France). Procedure blanks for Sr are <40 pg. No blank corrections have been applied to the analyzed ratio because blank contributions were insignificant in

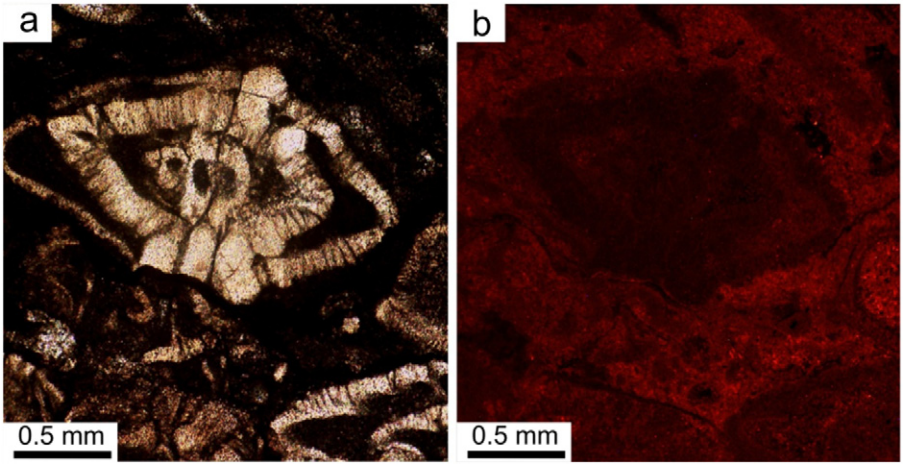

Fig. 5. Thin-section photomicrograph (a) and cathodoluminescence image (b) showing the main components (micrites and shell fragments of the larger foraminifera) in bulk carbonate and their weak luminescence.

comparison with the amount of respective elements in the sample. Strontium samples were loaded with Ta-emitter on Re filaments and analyzed by TIMS in the static multi-collection mode. Isotope ratios were normalized to $^{86}Sr/^{88}Sr$ of 0.1194. According to the NIST 987 standard material, the external reproducibility is $^{87}Sr/^{86}Sr$ of 0.710247 ± 14 (2SD, $n = 50$).

4. Results

4.1. The $\delta^{13}C_{carb}$ records

At Tingri, the $\delta^{13}C_{carb}$ values and their stratigraphical variations from both sections are very similar and show stepped CIE profiles (Fig. 4). The CIE profile can be subdivided into eight phases (**a**–**h**) according to changes in the slope of $\delta^{13}C_{carb}$ values. In our study, we use phases **a**–**b**, **c**–**g** and **h** to represent the pre-CIE, the main CIE and the CIE recovery, respectively.

In phase **a** (0–2.8 m), $\delta^{13}C_{carb}$ values decrease from ~3‰ to ~2.4‰. Upward, a slight, $\delta^{13}C_{carb}$ increase from ~2.4‰ to ~2.7‰ is observed in phase **b** (~2.8–7.6 m). Phase **c** at ~7.6 m marks the CIE onset and shows a decrease in $\delta^{13}C_{carb}$ values by ~3.5‰ within ~0.3 m-thick interval of the nodular limestone. The main CIE covers ~10.8 m of the sections and is characterized by a stepped decrease in $\delta^{13}C_{carb}$ values. The lowest $\delta^{13}C_{carb}$ value of −4.5‰ is recorded in the top of phase **g**. At ~18.4 m of the sections, a distinct, positive $\delta^{13}C_{carb}$ shift to values of −0.5‰ occurs at the bottom of phase **h**, which is followed by a more gradual rise in $\delta^{13}C_{carb}$ values to ~1‰. The total magnitude of the negative CIE at Tingri is ~7‰ (Fig. 4).

4.2. $CaCO_3$ concentration

Most of the samples are highly calcareous (>90 wt% $CaCO_3$). Below and above the main CIE, there are four intervals where wt% $CaCO_3$ falls below 90% due to an increase in terrigenous clay (i.e. marl layers). Within the main CIE, wt% $CaCO_3$ is very stable (92–96%) (Fig. 4).

4.3. Strontium and manganese content and $^{87}Sr/^{86}Sr$ ratios

Strontium concentrations vary from 400 ppm to 1900 ppm, clustering around ~800–1600 ppm. The Mn concentrations are ~40–200 ppm, with more than half of them below 70 ppm. The Mn/Sr ratios are <0.2, mostly ~0.03–0.14. The $^{87}Sr/^{86}Sr$ ratios are ~0.70777–0.70782 (Fig. 6b-d).

5. Discussion

5.1. Data evaluation

Diagenesis has the potential to strongly alter primary $\delta^{13}C_{carb}$ signals in the limestone. However, we are confident that the $\delta^{13}C_{carb}$ from Tingri is not significantly affected by diagenetic alteration, based on several lines of evidence. (1) Microscope inspections suggest good preservation of larger foraminifera and other fossils in the limestone (Fig. 5a). (2) Cathodoluminescence examination shows weak luminescence in the fossil fragments and the micritic parts (Fig. 5b). (3) In the $\delta^{13}C_{carb}$–$\delta^{18}O_{carb}$ cross-plot (Fig. 6a), the data from pre-CIE samples cluster in an area that indicates water-rock interaction within a closed system (Banner and Hanson, 1990). It implies that, although the $\delta^{18}O_{carb}$ values were altered, the primary $\delta^{13}C_{carb}$ values are still preserved. (4) Diagenesis usually causes a loss of Sr and an accumulation of Mn (Banner and Hanson, 1990). The studied limestone contains variably high Sr and low Mn concentrations, which also points to the water-rock interaction within a closed system (Fig. 6b). Furthermore, Mn/Sr ratios (<0.2) at Tingri are far below the empirical guideline (Mn/Sr < 1.5) that indicates good preservation of the primary $\delta^{13}C_{carb}$ signals (Kaufman et al., 1993), and the absence of the negative correlation between the Mn/Sr ratios and $\delta^{13}C_{carb}$ values shown in Fig. 6c also suggests the primary $\delta^{13}C_{carb}$ signals (Jacobsen and Kaufman, 1999). (5) The $^{87}Sr/^{86}Sr$ ratio in carbonate sediments/rocks is more susceptible to diagenesis than the $\delta^{13}C_{carb}$ (Bartley et al., 2001). Both values and temporal variations of the $^{87}Sr/^{86}Sr$ ratios from Tingri are consistent with those at ODP Sites 1262B and 1267B (Hodell et al., 2007) (Fig. 6d), where $\delta^{13}C_{carb}$ data have preserved primary signals (Zachos et al., 2005). Consequently, $\delta^{13}C_{carb}$ data from Tingri don't appear to be strongly altered by diagenesis.

At Tingri, the $\delta^{13}C_{carb}$ curves from two parallel sections do not completely overlap (Fig. 4), which implies that mixed different components in bulk carbonate should have affected the $\delta^{13}C_{carb}$ values. However, striking similarities in the stepped $\delta^{13}C_{carb}$ variations and in the CIE magnitude between two curves suggest that the mixing must have had an insignificant effect on the $\delta^{13}C_{carb}$ profiles so that two $\delta^{13}C_{carb}$ profiles can still exhibit almost identical expression of $\delta^{13}C_{carb}$ variations (Fig. 4).

Studies on some modern and ancient carbonate platforms suggest that seawater $\delta^{13}C$ in shallow epicontinental seas can be complicated by some local processes, such as freshwater discharge, evaporation, sea level changes and oxidation of organic matter (Immenhauser et al., 2008; Patterson and Walter, 1994). In such cases, it would lead to the decoupling of the carbon cycling in shallow epicontinental seas and in the open surface ocean (Immenhauser et al., 2008), and the $\delta^{13}C_{carb}$ records from shallow epicontinental seas cannot be representative of the carbon cycling in the open surface ocean (Immenhauser et al., 2008; Swart and Eberli, 2005). To test whether or not the $\delta^{13}C_{carb}$ records at Tingri were strongly altered by these local processes, we compare the $\delta^{13}C_{carb}$ data at Tingri with the $\delta^{13}C$ data of the mixed-layer foraminifer of *Acarinina* at ODP Sites that represent the surface seawater $\delta^{13}C$ in the open ocean. The comparison is focused on the pre-CIE interval, because the $\delta^{13}C$ records of *Acarinina* in the main CIE may be incomplete due to ocean acidification. In Fig. 7, the pre-CIE $\delta^{13}C_{carb}$ values at Tingri are, albeit slightly lower, generally in good agreement with the $\delta^{13}C$ values of *Acarinina* from ODP Sites 527, 689 and 690. It implies that these local processes that may affect water chemistry in some shallow epicontinental seas probably had negligible effects on the seawater $\delta^{13}C$ in the Tingri area, and the $\delta^{13}C_{carb}$ records at Tingri still preserve the carbon cycling signal in the open surface ocean.

5.2. The stepped CIE profile

Based on the discussions in Subsection 5.1, diagenesis, mixed different components and local processes are inferred to have had negligible effects on the $\delta^{13}C_{carb}$ records from Tingri. A final proof for the primary nature of $\delta^{13}C_{carb}$ variations in the studied sections would be the similarity of the observed stepped CIE profiles between Tingri and other regions (Fig. 8), which we demonstrate below.

At Tingri, the CIE profiles from both sections exhibit stepped $\delta^{13}C_{carb}$ variations with phases **a**-**h**. Generally, the stepped CIE profiles from Tingri are very similar to that from ODP Site 690 (Bains et al., 1999), except for phase **h** (Fig. 8).

In both sections from Tingri, the bottom of phase **h** is characterized by a sharp rise in $\delta^{13}C_{carb}$ values and is associated with abrupt lithological change from the nodular limestone to marl and with larger foraminiferal assemblage change (Fig. 4). The co-occurrence and abruptness of these changes indicate the presence of a stratigraphic hiatus, which is supported by the following observations. (1) The change of the foraminiferal assemblages from *Lockhartia*, *Miscellanea*, *Kathina*, *Operculina* and *Ranikothalia* to *Alveolina* suggests a shoaling of the depositional environment from 40 to 80 m to <40 m. (2) Microscopic evidence from thin-sections indicates that samples from this interval have undergone selective meteoric diagenesis, although such evidence is absent from the rest of these two sections. Both observations point to a period of subaerial exposure and support the interpretation of a hiatus at the

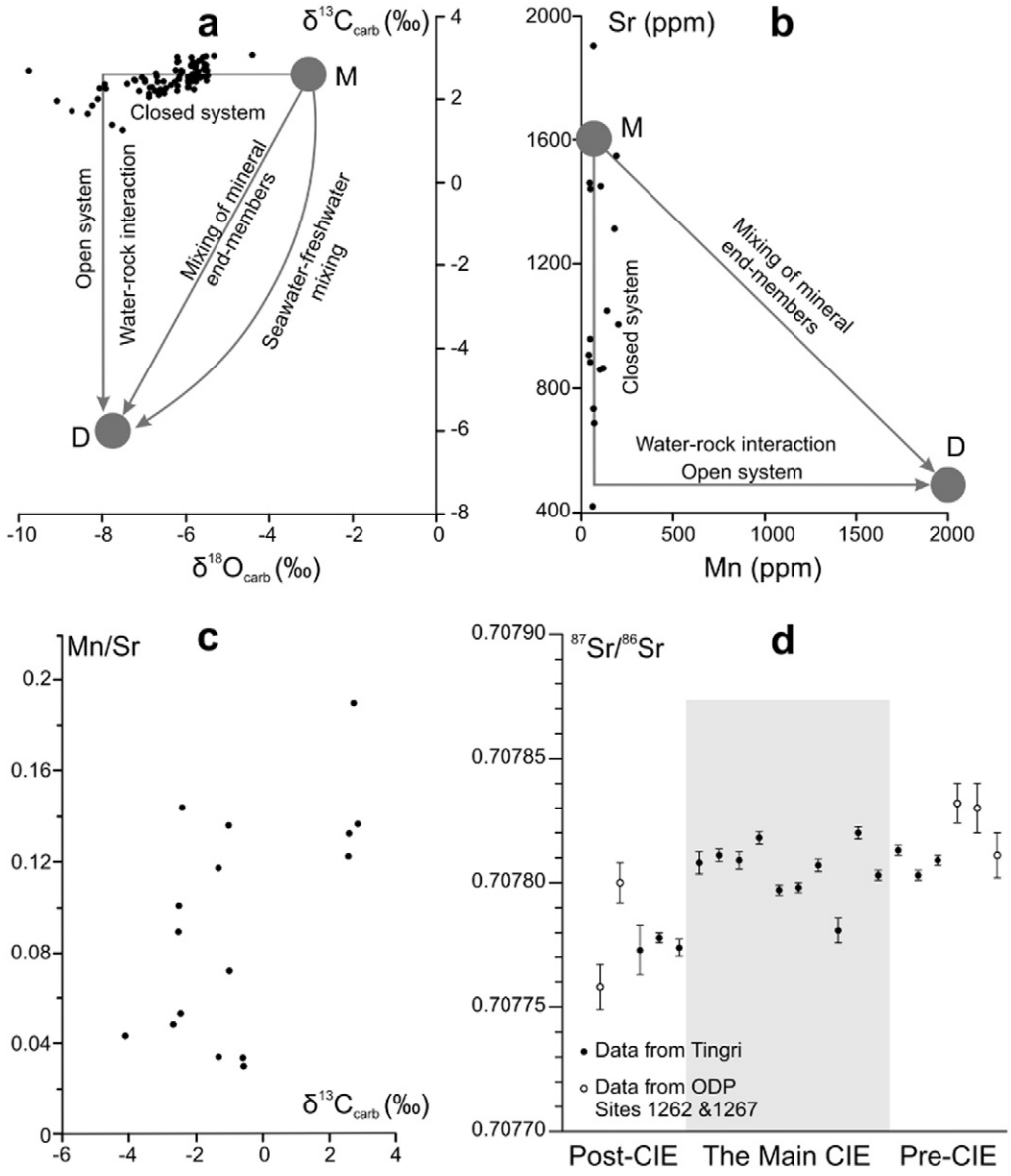

Fig. 6. Evaluation of diagenetic effects on the $\delta^{13}C_{carb}$ data from Tingri. (a) Cross-plot diagram of the $\delta^{13}C_{carb}$ and $\delta^{18}O_{carb}$ values from the pre-CIE samples. (b) Cross-plot diagram of Sr and Mn concentrations. (c) Cross-plot diagram of the Mn/Sr ratios and $\delta^{13}C_{carb}$ values. (d) Comparison of the $^{87}Sr/^{86}Sr$ ratios between Tingri (filled circles) and ODP Sites 1262B and 1267B (open circles). In (a) and (b), arrows represent different diagenetic pathways; 'M' and 'D' denote marine carbonate and diagenetic limestone, respectively. In (d), error bars show ± 1 standard deviation (SD).

onset of the CIE recovery. Therefore, our discussions in the following will be focused on the pre- and main intervals of the CIE.

In addition to ODP Site 690, $\delta^{13}C_{carb}$ variations from Tingri can further be correlated to those from the Nanyang Basin in China (Chen et al., 2014) and from the Mead Stream section in New Zealand (Nicolo et al., 2010). Surprisingly, they show very similar stepped CIE profiles by having most of the phases defined by Bains et al. (1999) (Fig. 8). One exception is phase **c** in the Nanyang Basin, where expression of the CIE onset is muted (Chen et al., 2014). Since the abrupt decrease in $\delta^{13}C$ values at the CIE onset is a key characteristic of the PETM (McInerney and Wing, 2011; Zachos et al., 2007) and was thought to reflect a sudden light carbon input into the atmosphere and ocean (Dickens et al., 1995), we tentatively infer that the CIE onset (phase **c**) in the Nanyang Basin might be not well preserved.

These four $\delta^{13}C_{carb}$ records are obtained from widely separated regions and reflect carbon isotope variations in very different depositional settings: a lake at Nanyang (Chen et al., 2014), a carbonate ramp at Tingri (Zhang et al., 2013), a continental slope at Mead Stream (Nicolo et al., 2010), and the open ocean at ODP Site 690 (Bains et al., 1999). Close similarity of these stepped CIE profiles suggests that they must reflect in detail the expression of the global carbon perturbation during the PETM, rather than the artifacts caused by diagenesis, mixed different components or other local processes. At ODP Site 690, the fact that the stepped CIE profile cannot be reproduced by the $\delta^{13}C$ measurements of foraminifera (Thomas et al., 2002) may be explained by preferential dissolution of the foraminifera (Chiu and Broecker, 2008) and/or mixed foraminifera of different ages due to bioturbation.

Comparison of the four stepped CIE profiles confirms that the main CIE consists of three phases (**c, e** and **g**) of large decreases in $\delta^{13}C_{carb}$ values, which are separated by two phases (**d** and **f**) of slight variations in $\delta^{13}C_{carb}$ values (Fig. 8). We interpret these large negative $\delta^{13}C_{carb}$ shifts in phases **c, e** and **g** to reflect three, discrete carbon release events (Fig. 8). This interpretation is consistent with the inferences from model simulations (Cui et al., 2011; Zeebe et al., 2009) and from boron isotope studies (Penman et al., 2014).

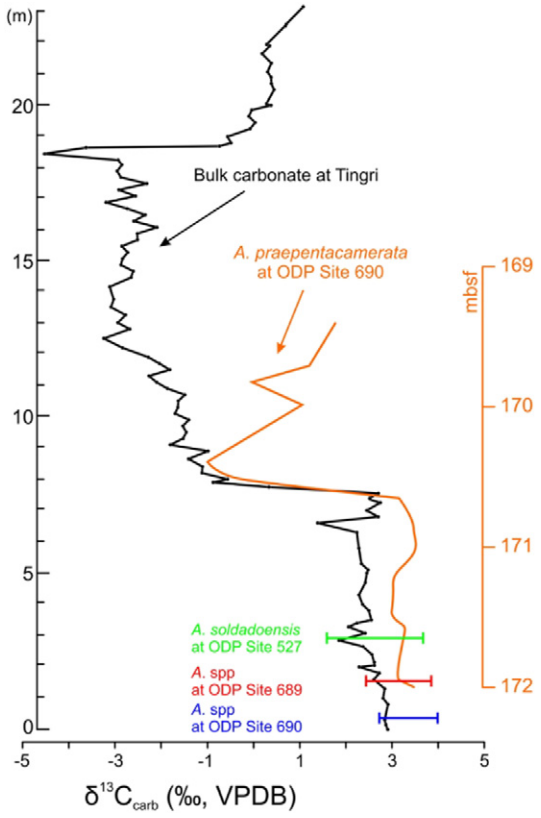

Fig. 7. Comparison of the pre-CIE $\delta^{13}C$ values of bulk carbonate at Tingri with those of *Acarinina* from different ODP Sites. At ODP Site 690, $\delta^{13}C$ values of *A. praepentacamerata* from Kennett and Stott (1991) are plotted versus depth in the core section. Three horizontal lines represent ranges of the pre-CIE $\delta^{13}C$ values of *Acarinina* at ODP sites 527, 689 and 690, sourced from Thomas et al. (1999), Zachos et al. (2007) and Thomas et al. (2002), respectively.

In phase **d**, $\delta^{13}C_{carb}$ values from ODP Site 690 are relatively constant, whereas they decrease steadily in the other three sections (Fig. 8). Owing to the inconsistent trends of $\delta^{13}C_{carb}$ variations, whether they reflect a carbon release event is still uncertain. In phase **e**, the detailed expression of the $\delta^{13}C_{carb}$ variations is different among these four sections. It shows several negative $\delta^{13}C_{carb}$ shifts in the Nanyang Basin, two shifts at Tingri and Mead Stream, and only one at ODP Site 690 (Fig. 8). It may reflect differences in temporal resolution among these sections, in relation to sample spacing and sedimentation rates. In phase **f**, the increasing $\delta^{13}C_{carb}$ values point to temporal dominance of negative feedback mechanisms that counteract the effects of light carbon release (Fig. 8).

5.3. The CIE magnitude

As discussed in Subsection 5.2, the stepped CIE profile most likely represents a more complete record of carbon perturbations during the PETM, compared to the simple, triangular CIE profile. Therefore, the full CIE magnitude can only be ascertained and studied from sections documenting the stepped CIE profile.

At Tingri, Mead Stream and ODP Site 690, the clear expression of the stepped CIE profiles indicates that the full magnitude of their local $\delta^{13}C$ fluctuations is captured. However, the CIE onset in the Nanyang Basin is strongly masked so that the observed value of ~4‰ can only represent the magnitude of the $\delta^{13}C$ shifts during phases **d** to **g**, not the full CIE magnitude. At the other three locations, the negative $\delta^{13}C$ shift in phase **c** accounts for about one third to half of their full CIE magnitude. Given that a similar percentage of the magnitude in phase **c** was also preserved in the Nanyang Basin, the full CIE magnitude would reach to ~6–8‰. This estimated value is consistent with the value of ~7‰ at Tingri, but larger than the value of ~2‰ at Mead Stream and ODP Site 690 (Fig. 8).

At ODP Site 690, the dominant components in bulk carbonate are calcareous nannofossils (Bains et al., 1999; Bralower, 2002; Stoll, 2005), and coccolithophores that produced these nannofossils should dwell in the photic zone. However, the CIE magnitude measured from bulk carbonate is evidently smaller than that from the surface-dwelling *Acarinina*, but identical to those from the thermocline-dwelling *Subbotina* and the benthic foraminifer *Nuttallides* (Bains et al., 1999; Kennett and Stott, 1991). To reconcile this contradiction, Stoll (2005) proposed that although coccolithophores and *Acarinina* must dwell in the photic zone, they need not have both inhabited in the mixed layer of the ocean. During the PETM, if the mixed layer at ODP Site 690 was very shallow and coccolithophores occupied a deep habitat below the mixed layer, it is possible that coccolithophores would record the carbon isotope signal similar to that of *Subbotina*, but different from that of *Acarinina*. A recent study on the genus *Discoaster*, one of the major coccolithophores from ODP Site 690 (Bains et al., 1999; Bralower, 2002; Stoll, 2005), suggested that the species of *Discoaster* preferred a deep habitat in the lower-photic zone (Schueth and Bralower, 2015). Moreover, we also note that the mixed layer depth in the modern Antarctic below ~60°S is <25 m (Kara et al., 2003), and ODP Site 690 was located at ~65°S in the Weddell Sea of the Antarctic during the PETM (Thomas et al., 1999). Given that the mixed layer depth during the PETM was not significantly different from that at present, the reconciliation given by Stoll (2005) appears to be plausible. So, we tentatively interpret the $\delta^{13}C_{carb}$ variations at ODP Site 690 as reflecting carbon isotope changes in the intermediate water, not the surface ocean.

Previous studies on foraminifera $\delta^{13}C$ from ODP Site 690 suggest that the CIE magnitude in the atmosphere and surface ocean was larger than that in the intermediate water and the deep ocean during the PETM (Zachos et al., 2007), and this suggestion is supported by the difference of the CIE magnitude between Nanyang Basin, Tingri and Mead Stream, ODP Site 690 (Fig. 8). However, the CIE magnitude of ~7‰ from Tingri is larger than the value of ~4‰ proposed for the full CIE magnitude in the atmosphere and the surface ocean (John et al., 2008; Zachos et al., 2007).

The CIE magnitude of ~4‰ at ODP Site 690 was obtained from $\delta^{13}C$ measurements of the mixed-layer foraminifer *Acarinina* (Kennett and Stott, 1991; Zachos et al., 2007), and the $\delta^{13}C$ data from *Acarinina* don't exhibit the stepped CIE profile (Fig. 7). During the PETM, it was suggested that the mixed-layer foraminifer would be preferentially dissolved on the ocean floor, compared to the more dissolution-resistant thermocline and benthic foraminifera (Zachos et al., 2007). It was further suggested that the foraminifera would be less resistant to dissolution than the coccoliths (Chiu and Broecker, 2008). At ODP Site 690, components forming the bulk carbonate are mainly composed of coccoliths and foraminifera (Kennett and Stott, 1991), and carbonate dissolution was confirmed to have occurred during the PETM, as evidenced by a decline in carbonate content from ~90% to ~60% and an increase in planktonic foraminiferal shell fragmentation (Kelly et al., 2005). Thus, the mixed-layer foraminifer *Acarinina* at ODP Site 690 cannot be completely preserved, and some *Acarinina* specimens must be dissolved so that the $\delta^{13}C$ data from the remaining *Acarinina* specimens do not display the stepped CIE profile. Likely, the *Acarinina* specimen recording the most negative $\delta^{13}C$ value might have escaped preservation. Thus, the value of ~4‰ from *Acarinina* at ODP Site 690 probably represents a conservative estimate on the CIE magnitude in the surface ocean, not the full magnitude.

Aside from ODP Site 690, ~4‰ of the negative CIE magnitude was also reported from the *Acarinina* at Bass River (New Jersey margin), where the $\delta^{13}C$ data show a triangular CIE profile (John et al., 2008). At Bass River, a lithological change from glauconite-rich silt to clay at the CIE onset likely points to the existence of a sedimentary hiatus. Besides, the sedimentation rates at Bass River were suggested to be higher than that at ODP Site 690, whereas the thickness of the main CIE

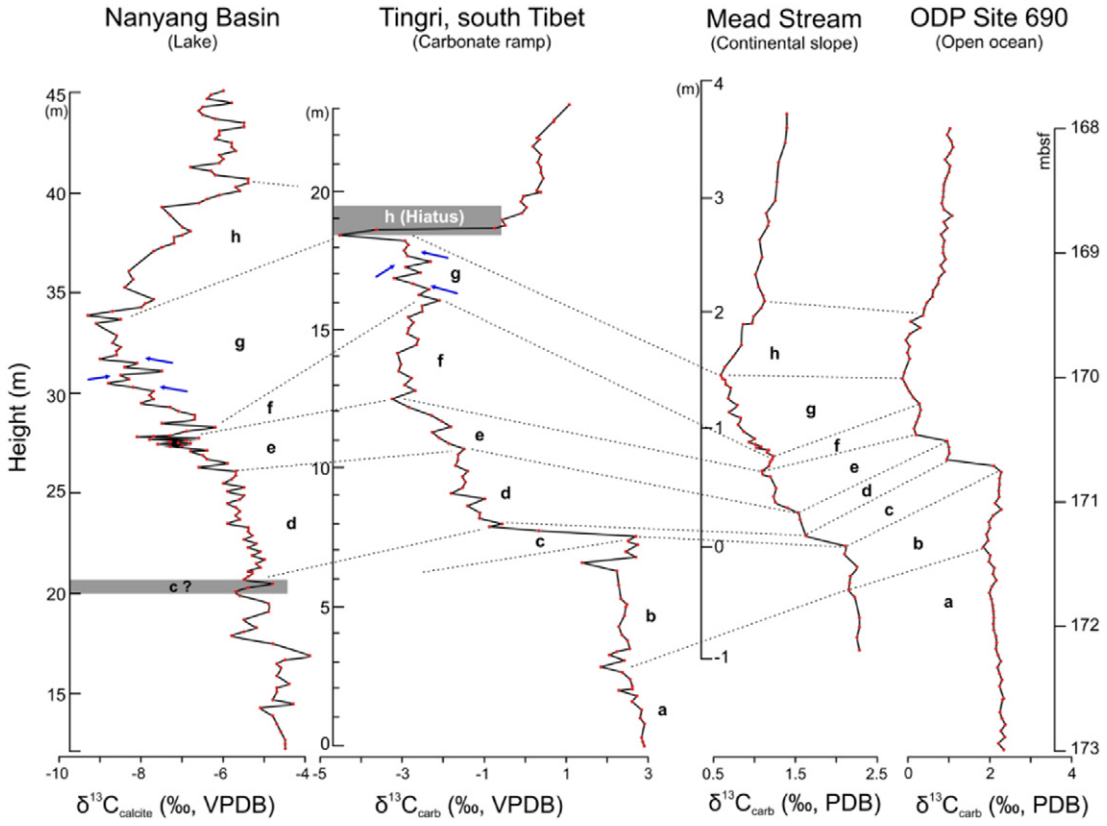

Fig. 8. Correlation of the stepped CIE profiles from four depositionally different environments. Note that small $\delta^{13}C$ variations within phase g (blue arrows) can be correlated between Nanyang basin and Tingri. Data sources are: for Nanyang basin from Chen et al. (2014), for Mead Stream from Nicolo et al. (2010), and for ODP Site 690 from Bains et al. (1999).

recorded in bulk carbonate at Bass River is thinner than that at ODP Site 690 (John et al., 2008), indicating an incomplete preservation of the sediments of the main CIE at Bass River. This inference is also consistent with the results from regional stratigraphic correlation in the New Jersey Coastal Plain (Stassen et al., 2012). Thus, the value of ~4‰ from the *Acarinina* at Bass River unlikely reflects the full CIE magnitude in the surface ocean, owing to the incomplete preservation of the main CIE.

Usually, the large CIE magnitude was suggested to be amplified by an increase in humidity, higher abundance of angiosperm flora or rising partial pressure of atmospheric carbon dioxide (Bowen et al., 2004; Smith et al., 2007; Schubert and Jahren, 2013). However, these mechanisms are only relevant to the large CIE magnitude measured from land-plants-related substrates, such as terrestrial organic matter, soil carbonate, plant lipids and tooth enamel. They cannot explain the CIE magnitude recorded in the lacustrine marls from the Nanyang basin or in the nodular limestone from Tingri. Moreover, if some local processes did amplify the CIE magnitude from the Nanyang basin and Tingri, they would also unavoidably alter the stepped CIE profiles so that this delicate CIE structure cannot be preserved. Apparently, the stepped CIE profiles from these two locations, particularly from Tingri, could rule out this possibility. In addition, the large CIE magnitude of ~7‰ is not only unique to Tingri, but was also reported from higher plant *n*-alkanes (~6‰) in the Arctic Ocean (Pagani et al., 2006) and bulk carbonate (~6–8‰) at Medford, Wilson Lake and Clayton on the Atlantic coastal plain (Wright and Schaller, 2013). So, we tentatively suggest that the magnitude of the negative CIE during the PETM might reach to ~7‰ in the atmosphere and the surface ocean, larger than the observed value of ~4‰ from *Acarinina* at ODP Site 690 and Bass River.

The larger CIE magnitude from the terrestrial and surface ocean records relative to that from the intermediate water and the deep ocean was widely reported (McInerney and Wing, 2011), and this difference was usually interpreted to be that either the large CIE magnitude was amplified (Bowen et al., 2004; Smith et al., 2007; Schubert and Jahren, 2013) or the small CIE magnitude was attenuated by incomplete preservation of the measured substrates (Pagani et al., 2006). However, the different CIE magnitude shown in the stepped CIE profiles from Tingri and ODP Site 690 cannot be the results of either amplification or attenuation, because the large CIE magnitude at Tingri is irrelevant to these amplifying mechanisms (Bowen et al., 2004; Smith et al., 2007; Schubert and Jahren, 2013) and the small CIE magnitude from bulk carbonate at ODP Site 690 is from a complete $\delta^{13}C_{carb}$ record.

Alternatively, this difference might be related to the propagation of the released light carbon in the ocean. Results from a model simulation suggest that it will take ~2–10 kyr for surface-injected passive tracers ($\delta^{13}C$, $\delta^{18}O$) to reach equilibrium in the modern ocean (Wunsch and Heimbach, 2008), which is much longer than as expected before (~1 kyr). Beside, the inferred strong ocean stratification during the PETM (Winguth et al., 2012) will further slow down the vertical mixing rate and facilitate the formation of the large difference in the CIE magnitude between the surface ocean and the deep ocean. In addition, a recent modeling study by using cGENIE (Kirtland Turner and Ridgwell, 2016) suggests that a rapid release of thousands of gigatons of ^{13}C–depleted carbon into the atmosphere can cause larger CIE magnitude in the atmosphere/the surface ocean and relatively smaller magnitude in the deep ocean. Although this modeling study investigated the consequences of a single carbon release, not multiple carbon releases, it can to some extent explain the large CIE magnitude at Tingri relative to the smaller magnitude at ODP Site 690.

6. Conclusions

In this study, we investigated the structure and magnitude of the CIE during the PETM. The investigation was based on expanded, high-resolution $\delta^{13}C_{carb}$ records from shallow marine carbonate sections at Tingri,

in conjunction with published $\delta^{13}C_{carb}$ records from other different regions. Our study suggests that the complete CIE record during the PETM should have a stepped structure, indicating multiple phases of carbon release. Large difference in the CIE magnitude, shown by the stepped CIE records from Tingri and ODP Site 690, confirms the larger $\delta^{13}C$ change in the surface ocean relative to the small change in the intermediate water and the deep ocean (Zachos et al., 2007). Besides, we tentatively propose that the magnitude of the negative CIE in the atmosphere and the surface ocean might be larger than the observed value of ~4‰ from *Acarinina* at ODP Site 690 and Bass River. We admit that both the CIE structure and magnitude at Tingri need be further refined by analyzing the $\delta^{13}C$ from larger foraminiferal shells, which can, to a greater extent, exclude possible effects of mixed different components on the $\delta^{13}C$ records.

Acknowledgements

We thank G. Dickens, A. Sluijs, C. Hollis, and five anonymous reviewers for comments on early versions of the manuscript and D. Penman for reviewing the manuscript, which improved our work significantly. We also thank F. Wieseler, S. Li, C. Wang, M. Kahsnitz and E. Leipprand for field work, and A. Hübner, C. Schott, P. Witte, A. Klügel, F. Lucassen, B. Kockisch and M. Segl for technical help in the laboratories. Funding for this research was provided by grants from the Chinese Academy of Sciences (XDB03010402), the National Natural Science Foundation of China (41490615), and the Deutsche Forschungsgemeinschaft (No. Wi725/29 and Wi725/26). The last project is part of the Priority Programme 1372 Tibetan Plateau: Formation, Climate, Ecosystems (*TiP*).

Appendix A. Supplementary data

Supplementary data to this article can be found online at http://dx.doi.org/10.1016/j.gr.2017.02.016.

References

Bains, S., Corfield, R.M., Norris, R.D., 1999. Mechanisms of climate warming at the end of the Paleocene. Science 285, 724–727.

Banner, J.L., Hanson, G.N., 1990. Calculation of simultaneous isotopic and trace element variations during water-rock interaction with applications to carbonate diagenesis. Geochimica et Cosmochimica Acta 54, 3123–3137.

Bartley, J.K., Semikhatov, M.A., Kaufman, A.J., Knoll, A.H., Pope, M.C., Jacobsen, S.B., 2001. Global events across the Mesoproterozoic-Neoproterozoic boundary: C and Sr isotopic evidence from Siberia. Precambrian Research 111, 165–202.

Bowen, G.J., Beerling, D.J., Koch, P.L., Zachos, J.C., Quattlebaum, T., 2004. A humid climate state during the Palaeocene/Eocene thermal maximum. Nature 432, 495–499.

Bralower, T.J., 2002. Evidence of surface water oligotrophy during the Paleocene-Eocene thermal maximum: Nannofossil assemblage data from Ocean Drilling Program Site 690, Maud Rise. Weddell Sea. Paleoceanography. http://dx.doi.org/10.1029/2001pa000662.

Chen, Z., Wang, X., Hu, J., Yang, S., Zhu, M., Dong, X., Tang, Z., Pa, Peng, Ding, Z., 2014. Structure of the carbon isotope excursion in a high-resolution lacustrine Paleocene-Eocene thermal maximum record from central China. Earth and Planetary Science Letters 408, 331–340.

Chiu, T., Broecker, W.S., 2008. Toward better paleocarbonate ion reconstructions: new insights regarding the $CaCO_3$ size index. Paleoceanography. http://dx.doi.org/10.1029/2008PA001599.

Cui, Y., Kump, L.R., Ridgwell, A.J., Charles, A.J., Junium, C.K., Diefendorf, A.F., Freeman, K.H., Urban, N.M., Harding, I.C., 2011. Slow release of fossil carbon during the Palaeocene-Eocene thermal maximum. Nature Geoscience 4, 481–485.

DeCelles, P.G., Robinson, D.M., Zandt, G., 2002. Implications of shortening in the Himalayan fold-thrust belt for uplift of the Tibetan Plateau. Tectonics. http://dx.doi.org/10.1029/2001TC001322.

DeConto, R.M., Galeotti, S., Pagani, M., Tracy, D., Schaefer, K., Zhang, T., Pollard, D., Beerling, D.J., 2012. Past extreme warming events linked to massive carbon release from thawing permafrost. Nature 484, 87–91.

Dickens, G.R., O'Neil, J.R., Rea, D.K., Owen, R.M., 1995. Dissociation of oceanic methane hydrate as a cause of the carbon isotope excursion at the end of the Paleocene. Paleoceanography 10, 965–971.

Dunkley Jones, T., Lunt, D.J., Schmidt, D.N., Ridgwell, A., Sluijs, A., Valdes, P.J., Maslin, M., 2013. Climate model and proxy data constraints on ocean warming across the Paleocene-Eocene thermal maximum. Earth-Science Reviews 125, 123–145.

Farley, K.A., Eltgroth, S.F., 2003. An alternative age model for the Paleocene-Eocene thermal maximum using extraterrestrial ^{3}He. Earth and Planetary Science Letters 208, 135–148.

Higgins, J.A., Schrag, D.P., 2006. Beyond methane: towards a theory for the Paleocene-Eocene thermal maximum. Earth and Planetary Science Letters 245, 523–537.

Hodell, D.A., Kamenov, G.D., Hathorne, E.C., Zachos, J.C., Röhl, U., Westerhold, T., 2007. Variations in the strontium isotope composition of seawater during the Paleocene and early Eocene from ODP Leg 208 (Walvis Ridge). Geochemistry, Geophysics, Geosystems. http://dx.doi.org/10.1029/2007gc001607.

Hollis, C.J., Hines, B.R., Littler, K., Villasante-Marcos, V., Kulhanek, D.K., Strong, C.P., Zachos, J.C., Eggins, S.M., Northcote, L., Phillips, A., 2015. The Paleocene-Eocene thermal maximum at DSDP Site 277, Campbell Plateau, southern Pacific Ocean. Climate of the Past 11, 1009–1025.

Hottinger, L., 1997. Shallow benthic foraminiferal assemblages as signals for depth of their deposition and their limitations. Bull Soc Géol Fr 168, 491–505.

Immenhauser, A., Holmden, C., Patterson, W.P., 2008. Interpreting the carbon-isotope record of ancient shallow epeiric seas: lessons from the recent. In: Pratt, B.R., Holmden, C. (Eds.), Dynamics of Epeiric Seas. Vol. 48. Geological Association of Canada, pp. 137–174.

Jacobsen, S.B., Kaufman, A.J., 1999. The Sr, C and O isotopic evolution of Neoproterozoic seawater. Chemical Geology 161, 37–57.

John, C.M., Bohaty, S.M., Zachos, J.C., Sluijs, A., Gibbs, S., Brinkhuis, H., Bralower, T.J., 2008. North American continental margin records of the Paleocene-Eocene thermal maximum: implications for global carbon and hydrological cycling. Paleoceanography. http://dx.doi.org/10.1029/2007PA001465.

Kara, A.B., Rochford, P.A., Hurlburt, H.E., 2003. Mixed layer depth variability over the global ocean. Journal of Geophysical Research. http://dx.doi.org/10.1029/2000JC000736.

Kaufman, A.J., Jacobsen, S.B., Knoll, A.H., 1993. The Vendian record of Sr and C isotopic variations in seawater: implications for tectonics and paleoclimate. Earth and Planetary Science Letters 120, 409–430.

Kelly, D.C., Zachos, J.C., Bralower, T.J., Schellenberg, S.A., 2005. Enhanced terrestrial weathering/runoff and surface ocean carbonate production during the recovery stages of the Paleocene-Eocene thermal maximum. Paleoceanography. http://dx.doi.org/10.1029/2005PA001163.

Kennett, J.P., Stott, L.D., 1991. Abrupt deep-sea warming, palaeoceanographic changes and benthic extinctions at the end of the Palaeocene. Nature 353, 225–229.

Kirtland Turner, S., Ridgwell, A., 2016. Development of a novel empirical framework for interpreting geological carbon isotope excursions, with implications for the rate of carbon injection across the PETM. Earth and Planetary Science Letters 435, 1–13.

Manners, H.R., Grimes, S.T., Sutton, P.A., Domingo, L., Leng, M.J., Twitchett, R.J., Hart, M.B., Dunkley Jones, T., Pancost, R.D., Duller, R., Lopez-Martinez, N., 2013. Magnitude and profile of organic carbon isotope records from the Paleocene-Eocene thermal maximum: evidence from northern Spain. Earth and Planetary Science Letters 376, 220–230.

McInerney, F.A., Wing, S.L., 2011. The Paleocene-Eocene thermal maximum: a perturbation of carbon cycle, climate, and biosphere with implications for the future. Annual Review of Earth and Planetary Sciences 39, 489–516.

Najman, Y., 2006. The detrital record of orogenesis: a review of approaches and techniques used in the Himalayan sedimentary basins. Earth-Science Reviews 74, 1–72.

Nicolo, M.J., Dickens, G.R., Hollis, C.J., 2010. South Pacific intermediate water oxygen depletion at the onset of the Paleocene-Eocene thermal maximum as depicted in New Zealand margin sections. Paleoceanography. http://dx.doi.org/10.1029/2009pa001904.

Pagani, M., Pedentchouk, N., Huber, M., Sluijs, A., Schouten, S., Brinkhuis, H., Sinninghe Damste, J.S., Dickens, G.R., the Expedition 302 Scientists, 2006. Arctic hydrology during global warming at the Palaeocene/Eocene thermal maximum. Nature 442, 671–675.

Patterson, W.P., Walter, L.M., 1994. Depletion of ^{13}C in seawater $\Sigma C0_2$ on modern carbonate platforms: significance for the carbon isotopic record of carbonates. Geology 22, 885–888.

Penman, D.E., Hönisch, B., Zeebe, R.E., Thomas, E., Zachos, J.C., 2014. Rapid and sustained surface ocean acidification during the Paleocene-Eocene thermal maximum. Paleoceanography. http://dx.doi.org/10.1002/2014pa002621.

Röhl, U., Westerhold, T., Bralower, T.J., Zachos, J.C., 2007. On the duration of the Paleocene-Eocene thermal maximum (PETM). Geochemistry, Geophysics, Geosystems. http://dx.doi.org/10.1029/2007gc001784.

Schubert, B.A., Jahren, A.H., 2013. Reconciliation of marine and terrestrial carbon isotope excursions based on changing atmospheric CO_2 levels. Nature Communications. http://dx.doi.org/10.1038/ncomms2659.

Schueth, J.D., Bralower, T.J., 2015. The relationship between environmental change and the extinction of the nannoplankton *Discoaster* in the early Pleistocene. Paleoceanography. http://dx.doi.org/10.1002/2015pa002803.

Serra-Kiel, J., Hottinger, L., Caus, E., Drobne, K., Ferràndez, C., Jauhri, A.K., Less, G., Pavlovec, R., Pignatti, J., Samsó, J.M., Schaub, H., Sirel, E., Strougo, A., Tambareau, Y., Tosequella, J., Zakrevskaya, E., 1998. Larger foraminiferal biostratigraphy of the Tethyan Paleocene and Eocene. Bull. Soc. Géol. Fr. 169, 281–299.

Sluijs, A., Dickens, G.R., 2012. Assessing offsets between the $\delta^{13}C$ of sedimentary components and the global exogenic carbon pool across early Paleogene carbon cycle perturbations. Global Biogeochemical Cycles. http://dx.doi.org/10.1029/2011gb004224.

Smith, F.A., Wing, S.L., Freeman, K.H., 2007. Magnitude of the carbon isotope excursion at the Paleocene-Eocene thermal maximum: the role of plant community change. Earth and Planetary Science Letters 262, 50–65.

Stassen, P., Thomas, E., Speijer, R.P., 2012. Integrated stratigraphy of the Paleocene-Eocene thermal maximum in the New Jersey Coastal Plain: toward understanding the effects of global warming in a shelf environment. Paleoceanography. http://dx.doi.org/10.1029/2012PA002323.

Stoll, H.M., 2005. Limited range of interspecific vital effects in coccolith stable isotopic records during the Paleocene-Eocene thermal maximum. Paleoceanography. http://dx.doi.org/10.1029/2004pa001046.

Svensen, H., Planke, S., Malthe-Sorenssen, A., Jamtveit, B., Myklebust, R., Rasmussen Eidem, T., Rey, S.S., 2004. Release of methane from a volcanic basin as a mechanism for initial Eocene global warming. Nature 429, 542–545.

Swart, P.K., Eberli, G., 2005. The nature of the $\delta^{13}C$ of periplatform sediments: implications for stratigraphy and the global carbon cycle. Sediment. Geol. 175, 115–129.

Thomas, D.J., Bralower, T.J., Zachos, J.C., 1999. New evidence for subtropical warming during the Late Paleocene thermal maximum: stable isotopes from Deep Sea Drilling project Site 527, Walvis Ridge. Paleoceanography 14, 561–570.

Thomas, D.J., Zachos, J.C., Bralower, T.J., Thomas, E., Bohaty, S., 2002. Warming the fuel for the fire: evidence for the thermal dissociation of methane hydrate during the Paleocene-Eocene thermal maximum. Geology 30, 1067–1070.

Willems, H., Zhou, Z., Zhang, B., Gräfe, K.U., 1996. Stratigraphy of the upper cretaceous and lower tertiary strata in the Tethyan Himalayas of Tibet (Tingri area, China). Geologische Rundschau 85, 723–754.

Winguth, A.M.E., Thomas, E., Winguth, C., 2012. Global decline in ocean ventilation, oxygenation, and productivity during the Paleocene-Eocene thermal maximum: implications for the benthic extinction. Geology 40, 263–266.

Wright, J.D., Schaller, M.F., 2013. Evidence for a rapid release of carbon at the Paleocene-Eocene thermal maximum. Proc. Natl. Acad. Sci. 110, 15908–15913.

Wunsch, C., Heimbach, P., 2008. How long to oceanic tracer and proxy equilibrium? Quat. Sci. Rev. 27, 637–651.

Zachos, J.C., Wara, M.W., Bohaty, S., Delaney, M.L., Petrizzo, M.R., Brill, A., Bralower, T.J., Premoli-Silva, I., 2003. A transient rise in Tropical Sea surface temperature during the Paleocene-Eocene thermal maximum. Science 302, 1551–1554.

Zachos, J.C., Röhl, U., Schellenberg, S.A., Sluijs, A., Hodell, D.A., Kelly, D.C., Thomas, E., Nicolo, M., Raffi, I., Lourens, L.J., McCarren, H., Kroon, D., 2005. Rapid acidification of the ocean during the Paleocene-Eocene thermal maximum. Science 308, 1611–1615.

Zachos, J.C., Bohaty, S.M., John, C.M., McCarren, H., Kelly, D.C., Nielsen, T., 2007. The Palaeocene–Eocene carbon isotope excursion: constraints from individual shell planktonic foraminifer records. Philosophical Transactions of the Royal Society A 365, 1829–1842.

Zeebe, R.E., Zachos, J.C., Dickens, G.R., 2009. Carbon dioxide forcing alone insufficient to explain Palaeocene-Eocene thermal maximum warming. Nature Geoscience 2, 576–580.

Zhang, Q., Willems, H., Ding, L., 2013. Evolution of the Paleocene-Early Eocene larger benthic foraminifera in the Tethyan Himalaya of Tibet, China. International Journal of Earth Sciences 102, 1427–1445.

Zhu, M., Ding, Z., Wang, X., Chen, Z., Jiang, H., Dong, X., Ji, J., Tang, Z., Luo, P., 2010. High-resolution carbon isotope record for the Paleocene-Eocene thermal maximum from the Nanyang Basin, Central China. Chinese Science Bulletin 55, 3606–3611.